applied sciences

MDPI

Article

Ground Settlement Analysis of Twin Shield Tunnels Under River-Crossing Conditions with Fluid–Solid Coupling

Jiahui Tang *, Zhiwen Ran and Xianghong Ding

College of Civil Engineering, Zhejiang University of Technology, Hangzhou 310023, China
* Correspondence: 211123060021@zjut.edu.cn

Abstract

Twin shield tunneling in river-crossing soft soils faces increased risks like face instability, largely due to unclear mechanisms linking water level fluctuations to ground settlement. To address this issue, a 3D fluid–solid-coupled FLAC3D model is developed based on the Zhanqiaogang section of Hangzhou Metro Line 15. Specifically, the model simulates four hydrological conditions: low water, normal water level, high water level, and flood level. It examines their effects on ground settlement, stress distribution, and pore water pressure during twin-tunnel excavation. The results indicate that the maximum ground surface settlement on the left alignment under flood-level conditions increased by 41.58% compared with that under normal water levels. On the right alignment, surface settlement increased from 6.54 mm under normal water levels to 8.54 mm under flood conditions, representing a 30.6% increase. A sensitivity analysis is also conducted on pore water pressure, soil internal friction angle, and support stiffness. Results show that ground settlement increases with rising river levels, mainly due to elevated pore pressure reducing soil strength. Sensitivity analysis confirms pore pressure as the key factor influencing deformation. Numerical results align well with field data, highlighting the critical role of hydraulic boundaries. Based on these results, control measures are proposed to provide practical guidance for mitigating settlement in similar river-crossing tunnel projects.

Keywords: twin tunnels; fluid–solid coupling; sensitivity analysis; numerical simulation; tunnelling beneath a river

1. Introduction

With the acceleration of global urbanization, surface traffic congestion has become increasingly severe, prompting the rapid development of underground transportation systems [1–3]. Shield tunnelling has emerged as the predominant method for constructing urban metro lines due to its high efficiency and construction safety [4–6]. These alignments often pass beneath rivers, lakes, and other water bodies. Such underwater tunnelling projects pose significant challenges, characterized by high hydrostatic pressure and complex geological conditions, particularly in soft soil strata [7–9]. When crossing riverbeds under shallow cover, both the shield machine and the completed tunnel are prone to axial misalignment, manifested by shield uplift, difficulty in maintaining excavation face stability, tunnel flotation leading to localized deformation, opening of segment joints, and water leakage. Severe accidents such as excavation face instability and collapse or even lake water penetrating the ground and inundating the tunnel may occur, posing significant safety risks to tunnel advancement. During underground excavation operations requiring worker access, ensuring the sustained stability of tunnels has long been a focal issue in

Check for updates

Academic Editor: Tiago Filipe da Silva Miranda

Received: 18 January 2026
Revised: 16 February 2026
Accepted: 22 February 2026
Published: 25 February 2026

Copyright: © 2026 by the authors. Licensee MDPI, Basel, Switzerland. This article is an open access article distributed under the terms and conditions of the Creative Commons Attribution (CC BY) license.

underground engineering construction and research [10]. Given these concerns, accurately predicting and controlling ground deformation induced by river-crossing shield tunnelling is critical for the sustainable development of urban infrastructure [11,12].

The mechanism of ground deformation during underwater tunnel excavation is governed by the complex interaction between the soil skeleton and pore water, known as fluid–solid coupling (or hydro-mechanical coupling). Tunnel excavation disturbs the in situ geostress and hydraulic fields, leading to pore water pressure dissipation and redistribution of effective stress, which in turn induces soil deformation and ground settlement [13,14]. Extensive research has been conducted on this issue [15]. For example, Shariful Islam et al. [16] systematically studied the surface settlement behavior of stacked twin tunnels using 3D finite element analysis (MIDAS GTS NX), evaluating the effects of cover-to-span ratio (C/D), pier-to-span ratio (P/D), and excavation sequence, and proposed design charts for settlement prediction. Hao et al. [17] combined FLAC3D simulation with field monitoring to analyze stress distribution and surface settlement when tunnels pass beneath buildings. They clarified the expansion pattern of settlement troughs and structural stress thresholds, providing a basis for risk control in such scenarios. In terms of long-term behavior, Huang et al. [18] simulated construction-induced settlement and validated the results against field data, demonstrating effective settlement control and recommending mitigation measures such as slurry modification and simultaneous grouting. Liu et al. [19], used long-term monitoring data from the Zhengzhou Metro and applied a logistic curve model to predict settlement in saturated sandy soils. Their results revealed an S-shaped, time-dependent settlement pattern and highlighted the influence of hydrogeological conditions, offering a simple yet effective tool for long-term prediction. Regarding water-rich tunnel failures, Ma et al. [20] conducted field investigations of several incidents in China, back-analyzed the ultimate water pressure using FLAC3D, and proposed countermeasures including support reinforcement and drainage system optimization. However, most existing studies have been conducted under static or simplified groundwater conditions [21–23]. Although the importance of water pressure is widely acknowledged, the impact of dynamic water level fluctuations in rivers and lakes, as a critical hydraulic boundary condition, has not been systematically or quantitatively explored using fluid–solid coupling analysis [24,25]. In particular, the dynamic response of twin tunnels under varying river water levels and the coupled influence of the first-excavated tunnel on the second remain insufficiently understood.

This study develops a three-dimensional numerical model incorporating fluid–solid coupling using FLAC3D, based on the river-crossing section of Hangzhou Metro Line 15 beneath the Zhanqiaogang River. By simulating the full excavation process of twin tunnels under four different river water levels (low, normal, high, and flood stages), the model systematically explores how dynamic hydraulic boundaries affect surface settlement, surrounding soil stress, and pore water pressure. A sensitivity analysis is performed to identify key controlling factors. This research aims to uncover the underlying mechanisms of tunnel deformation under high water pressure in river-crossing conditions and provides theoretical support and technical guidance for risk assessment, design optimization, and construction safety in similar projects.

2. Engineering Background

The Phase 1 project of Hangzhou Metro Line 15 includes the Longteng Street Station to Zhanjiaqiao Road Station section, which consists of a twin-tunnel alignment. In this section, the right-line tunnel is 765.060 m and the left-line tunnel is 799.897 m, starting at YDK49 + 709.777, and ending at YDK50 + 474.837, The section from YDK50 + 063.303 to YDK50 + 126.193 intersects with the Zhanqiaogang River channel. This section was

constructed using two composite earth pressure balance (EPB) shield machines, launching from Longteng Station and arriving at Zhanjiaqiao Road Station, as shown in Figure 1. The shield tunnel has a circular cross-section with an outer diameter of 6200 mm and an inner diameter of 5500 mm. During the undercrossing of the Zhanqiaogang River, a steel pipe mesh was laid at the riverbed, with waterproof membranes placed on top to block direct pathways between surface water and the tunnel [26,27]. This ensured smooth surface water flow over the tunnel crown during construction, thereby reducing the risk of water inflow or backflow into the tunnel in the event of localized collapses.

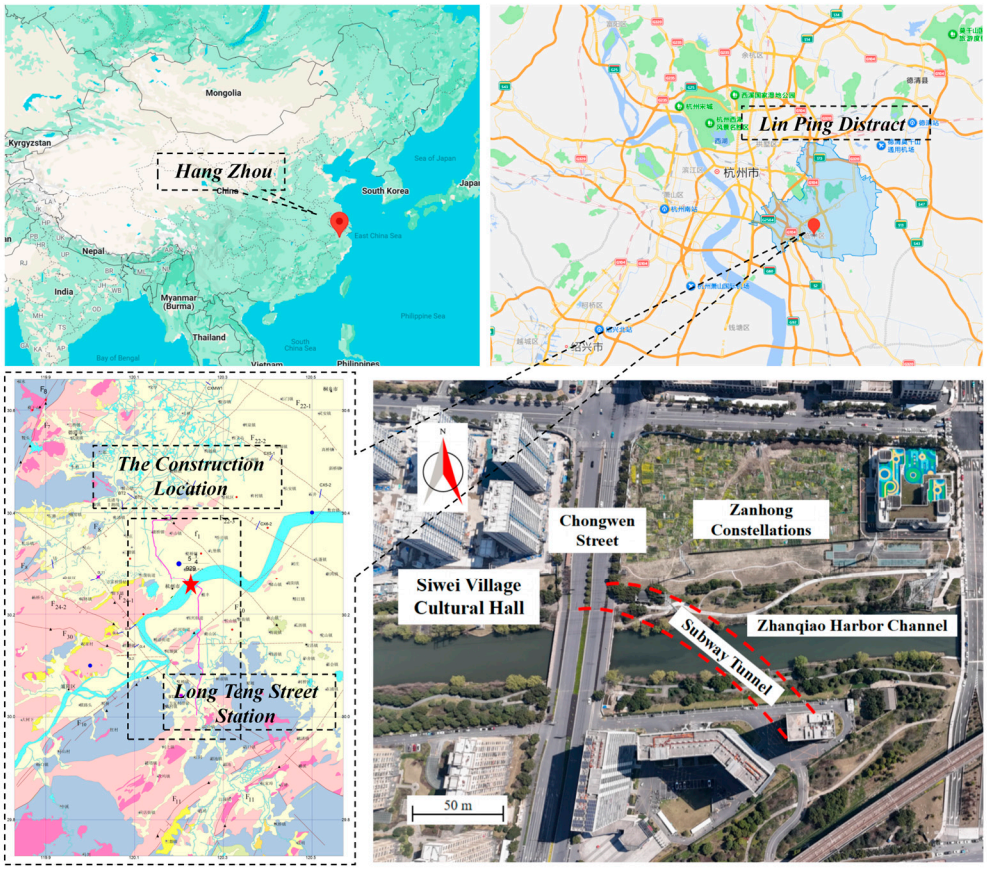


Figure 1. Location schematic diagram of shield tunnel. The dotted lines denote geographical names and delineate boundaries, while the pentagram indicates the precise position. The lower right corner shows an enlarged view of this location.

According to the engineering geological survey, the tunnel-surrounding soil is classified as Grade VI. The surface layer of the riverbed is generally covered with pond silt. This soil layer is typically brownish-gray to dark gray, wet, extremely soft, and rich in humus and plant roots. In some areas, small amounts of gravel and cobbles may be mixed in, with the main fill material being silty soil. The middle part consists of silty clay, silty clay with silt interlayers, and clayey silt formed by Holocene alluvial–lacustrine and marine deposits. The soil properties are moderate, and the distribution is relatively stable.

3. Methodology

3.1. Fluid–Solid Coupling

Dewatering during geotechnical construction alters the groundwater distribution, resulting in a redistribution of effective stress within the soil mass. The changes in the effective stress field, in turn, influence groundwater movement. This interaction between the stress field and the seepage field is referred to as fluid–solid coupling [28]. Essentially, it

involves deformation of the soil skeleton caused by the dissipation of pore water pressure. Under the assumption that soil particles are incompressible, soil deformation mainly arises from pore space compression. In this study, FLAC3D was used to simulate tunnel excavation beneath a river channel. During the hydro-mechanical coupling process, rising water levels lead to increased pore water pressure, which reduces the effective stress and shear strength of the soil, ultimately resulting in greater plastic deformation and settlement.

3.1.1. Governing Equations of Solid Mechanics

The constitutive model of soil is a mathematical expression relating stress, strain, strength, and time, and it reflects the mechanical behavior of the soil. In rheological theory, deformation characteristics are described by the relationship between deformation and time under a given stress [29]. In this study, the soil is regarded as an elasto-plastic material, and its total strain increment ($d\varepsilon_v$) is decomposed into three components, elasto-plastic ($d\varepsilon^{ep}$), viscoelastic ($d\varepsilon^{ve}$), and viscoplastic ($d\varepsilon^{vp}$) parts [30], as expressed below:

$$d\varepsilon_v = d\varepsilon^{ep} + d\varepsilon^{ve} + d\varepsilon^{vp} \tag{1}$$

3.1.2. Governing Equations of Fluid Seepage

Under hydro-mechanical coupling, the mechanical behavior of tunnels or soil interacting with fluid is governed by the equilibrium equation, while fluid flow is governed by the continuity equation. The equilibrium equation ensures the mechanical response of the solid skeleton under external forces and pore pressure, describing the stress-deformation balance within the soil. The continuity equation describes the conservation of mass of the fluid in porous media, i.e., the principle of constant volume during fluid flow in pores [31]. For small deformations, the fluid particle equilibrium equation is given as:

$$-q_{i,i} + q_v = \frac{\partial \zeta}{\partial t} \tag{2}$$

where $q_{i,i}$ is the seepage velocity, q_v is the fluid source strength per unit measured volume, and ζ is the volumetric fluid content change per unit volume of the porous medium.

$$\frac{\partial \zeta}{\partial t} = \frac{1}{M}\frac{\partial p}{\partial t} + \alpha\frac{\partial \varepsilon}{\partial t} - \beta\frac{\partial T}{\partial t} \tag{3}$$

where M is the Biot modulus, p is the pore pressure, α is the Biot coefficient, ε is the volumetric strain, β is the thermal expansion coefficient considering both fluid and solid particles, and T is the temperature.

When fluid flows through a porous medium, it primarily induces changes in pore water pressure, saturation, and seepage. The flow behavior of the fluid is described through the relationship between these variables and the fluid particle equilibrium equation in conjunction with Darcy's law [32]. For a homogeneous, isotropic solid and a fluid with constant density, the governing equation can be expressed as:

$$q_i = -k_{il}\hat{k}(s)\left[p - \rho_f x_j g_j\right] \tag{4}$$

where q_i is the seepage velocity, k_{ij} is the absolute permeability coefficient, $\hat{k}(s)$ is the relative permeability coefficient, p is the pore water pressure, ρ_f is the fluid density, and g_j is the gravitational acceleration.

3.1.3. Bidirectional Coupling Mechanism

Rock and soil are regarded as porous media, in which fluid flow follows Darcy's law. The fluid–solid coupling process is governed by Biot's equations. The complete fluid continuity equation incorporates Darcy's law, while Biot's theory links fluid flow to deformation of the solid matrix. The two-way coupling mechanism is manifested as follows: (1) changes in pore pressure directly affect the effective stress of the soil skeleton, thereby inducing soil deformation; (2) deformation of the soil skeleton alters the pore volume, leading to changes in pore water pressure; (3) fluid–solid coupling induces foundation settlement: when groundwater levels fluctuate or loading conditions change, pore pressure decreases, leading to reductions in effective stress and shear strength of the soil, which ultimately results in foundation settlement. In this process, the river acts as a dynamic hydraulic boundary that adjusts regional seepage boundary conditions and local seepage forces, thereby regulating the spatial gradient of pore pressure and influencing the redistribution of the effective stress field—serving as a critical external factor in slope instability and foundation settlement.

This coupling relationship can be established through Biot's consolidation theory, which is based on the following fundamental assumptions:

(1) The soil is a homogeneous, saturated elastic material;
(2) Soil deformation is assumed to be small;
(3) Soil particles and pore water are incompressible;
(4) Seepage obeys Darcy's law;
(5) Principal stresses vary with time.

The equation describing the Biot modulus is given as follows [33]:

$$M = \frac{K_f}{n + (\alpha - n)(1 - \alpha)K_f - K} \tag{5}$$

where M is the Biot modulus, K_f is the bulk modulus of the fluid, K is the bulk modulus of the drained porous material, n is the porosity of the material, and α is the Biot coefficient, defined as the ratio of fluid volume gained (or lost) within a material element to the volumetric change of that element under a change in pore pressure, where the default value is 1. Its value ranges between 0 and 1. The closer it is to 1, the less compressible the material.

3.2. Ground Settlement Theory Induced by Tunnel Volume Loss

Methods for estimating settlement induced by tunnel construction include empirical formulas, theoretical analysis, numerical simulations, and physical modeling. The most representative empirical method is the Peck formula. Based on years of field observations, Peck was the first to propose that the settlement profile perpendicular to the tunnel axis can be described using a Gaussian distribution curve. Peck suggested that ground settlement results from volume loss under undrained conditions, and thus the volume of the settlement trough is equal to the ground loss [34]. The formula used to predict surface settlement induced by tunneling is given as follows:

$$S(x) = S_{\max} \exp\left(-\frac{x^2}{2i^2}\right) \tag{6}$$

where $S(x)$ is the ground surface settlement, $S_{\max}$ is the maximum settlement at the tunnel centerline, x is the horizontal distance from the tunnel centerline, and i is the settlement trough width parameter.

Fang et al. [35], based on Peck's empirical formula for surface settlement induced by a single tunnel, proposed that the additional settlement trough induced by the second tunnel is assumed to be approximately symmetrical with respect to its centerline, and can also be described using a Gaussian function, as shown in Figure 2. The total settlement trough induced by twin tunnels can be obtained by superimposing the settlement troughs generated by each tunnel, as follows:

$$S = S_{\max 1} \exp\left[-\frac{x^2}{2i_1^2}\right] + S_{\max 2} \exp\left[-\frac{(x - L_x)^2}{2i_2^2}\right] \quad (7)$$

where i_1 and i_2 represent the settlement trough widths of the first and second tunnels, respectively, and Lx is the horizontal distance between the centerlines of the twin tunnels.

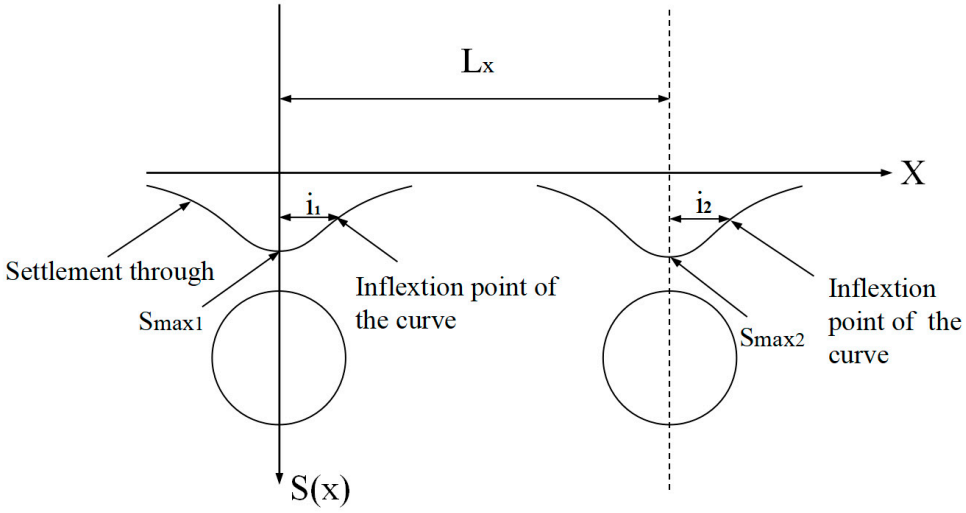


Figure 2. Surface settlement trough.

3.3. Computational Models and Parameters

The diameter of the circular metro tunnel is 6.20 m, and the center-to-center distance between the left and right tunnels is 31.29 m. The minimum clearance from the riverbed to the top of the shield tunnel is 8.73 m, which exceeds one tunnel diameter, and by controlling the excavation speed and the face pressure, the influence range on the segmental tunnel structure can be effectively limited.

Based on actual conditions, the model dimensions were reasonably defined. In this numerical simulation, Rhino 6 was used for 3D modeling, meshing was performed with Griddle, and the mesh data were imported into FLAC3D for computation and post-processing, as shown in Figure 3. According to elastoplastic rock mechanics theory, excavation of a circular tunnel affects the surrounding soil stress field within a range of 3 to 5 times the tunnel diameter, beyond which stress disturbance is less than 5% [36]. The computational width in the horizontal direction was set to approximately 5 times the tunnel diameter, and the vertical depth was set to 4 times the tunnel diameter. The final model dimensions were set to 100 m × 100 m × 40 m. To ensure the reliability of the numerical analysis results, the mesh was uniformly divided, resulting in a total of 410,600 zones and 425,715 gridpoints. In this modeling, the Mohr-Coulomb elastoplastic constitutive model was adopted [37]. This model, which focuses on shear failure, effectively captures the yield and strength behavior of geomaterials under loading. The model is computationally efficient and widely applied in geotechnical engineering problems such as slopes, tunnels, and foundations [38–40].



(**a**) Cross-sectional view of the tunnel (**b**) Tunnel 3D model

Figure 3. Schematic diagram of the tunnel.

Defining boundary and initial conditions for the numerical model is essential to ensure the accuracy and reliability of the simulation, and is a necessary step in solving the modeling problem. Specifically, the initial displacement, stress, and water level conditions are defined as follows [41]:

$$S(x, y, z, t)|_{t=0} = 0 \tag{8}$$

$$\sigma_{cz} = \gamma_s z; \sigma_{cx} = \sigma_{cy} = K_0 \gamma_s z \tag{9}$$

$$H(x, y, z, t)|_{t-0} = H_0(x, y, z) \tag{10}$$

where S is displacement, K_0 is the lateral earth pressure coefficient, σ_{cx}, σ_{cy}, σ_{cz} represent the stresses in the x, y, and z directions, respectively, γ_s is the bulk density of the soil, z is the computational depth, and H_0 denotes the initial groundwater level condition.

To realistically reflect the actual engineering conditions, the model was configured with the following boundary conditions. Mechanical boundary conditions: The bottom surface is fixed, the four lateral surfaces are constrained in the normal direction, and the top surface is a free boundary. Seepage boundary conditions: The model surface is set as a permeable boundary, while the bottom and all four sides are defined as impermeable boundaries. The initial pore water pressure is calculated using the hydrostatic pressure formula, taking into account the soil permeability and porosity.

In FLAC3D, numerical simulation is implemented through a series of computational cycles. Each cycle includes the following key steps: setting excavation boundary conditions, removing the excavated tunnel section, applying initial support, and installing the secondary lining. The computational strategy for this model is as follows: initially activate the seepage calculation process while deactivating the mechanical calculation; subsequently, deactivate the seepage process and activate the mechanical computation. The simulation defines an excavation advance of 2 m per computational cycle. From step 1 to step 50, the left tunnel is excavated; from step 51 to step 100, the right tunnel is excavated, completing a total of 100 excavation steps for both tunnels.

To facilitate result analysis, a typical cross-section at y = 50 m is selected within the tunnel for data extraction.

Calculation Parameters

Through field borehole sampling, in situ testing, geophysical exploration, and integration of existing data, a comprehensive and accurate set of geotechnical parameters of the foundation soil at the project site was obtained [42–44]. According to the site investigation

data provided in the geotechnical report by the construction unit, the stratigraphic and support parameters used in the numerical model are summarized in Table 1.

Table 1. Stratigraphic and Support Parameters.

Name	Thickness (m)	Unit Weight (KN/m^3)	Elastic Modulus (MPa)	Poisson's Ratio	Internal Friction Angle (°)	Cohesion (kPa)	Permeability Coefficient (m^2/Pa·s)
Silty Fill	0.6	18.1	2.3	0.42	8.0	8.0	3.1×10^{-9}
Silty Clay	3	18.4	7.6	0.40	13.2	25.5	5.61×10^{-8}
Silty Clay with Interlayers of Silt	10	18.9	10.6	0.37	14.7	29.7	4.76×10^{-8}
Silty Clay	7	19.5	14.6	0.34	16.6	34.5	4.63×10^{-8}
Clay	19.4	19.3	14.4	0.34	17.4	36.5	2.7×10^{-9}
Primary Support	0.05	24.0	2.68×10^4	0.3	—	—	—
Secondary Lining	0.30	24.2	3.0×10^4	0.2	—	—	—

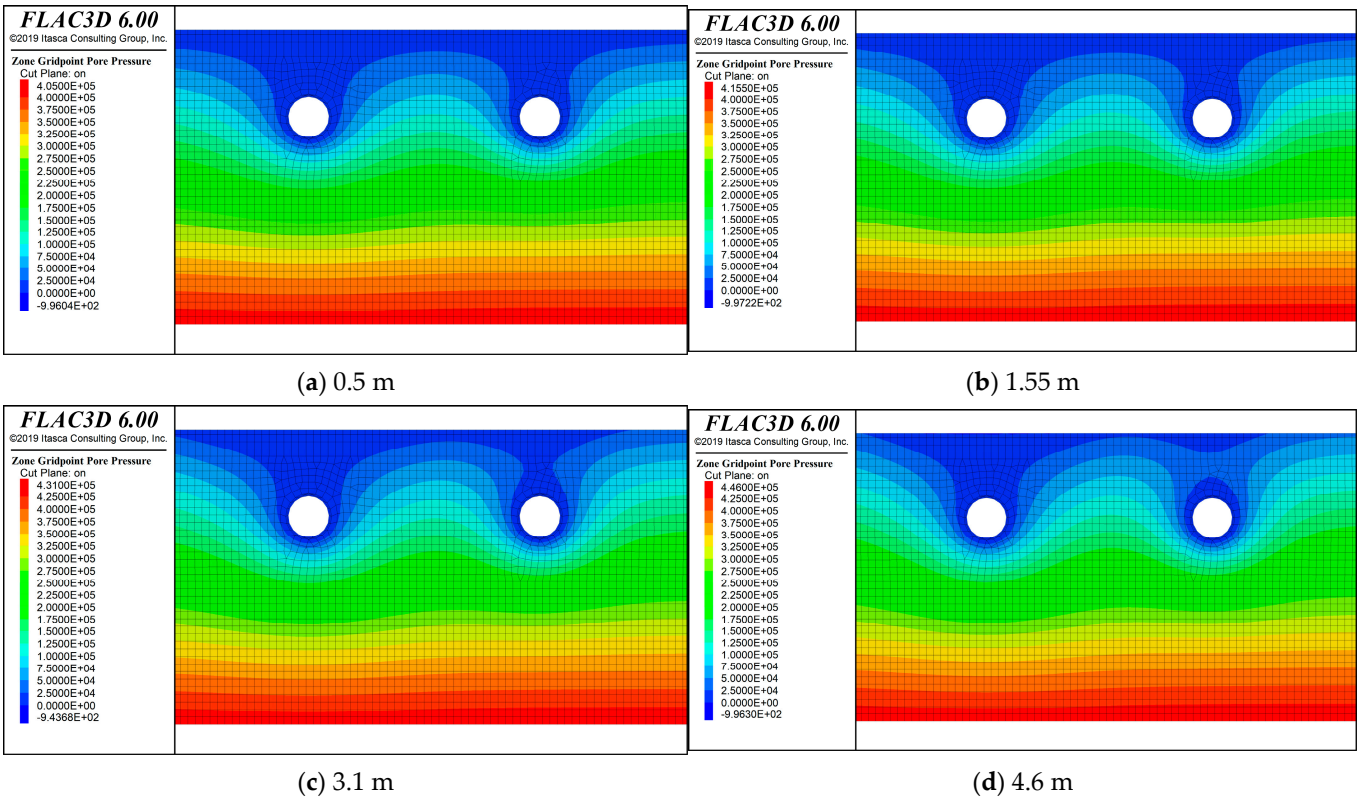
4. Result

The Zhanqiao Port River is 35 to 45 m wide and flows from north to south, with a flow velocity of 0.1 to 0.3 m/s. The normal water level is 1.55 m, and the historical maximum flood level is 4.6 m. The construction period for the shield tunnel crossing beneath the Zhanqiao Port River is relatively long and may encounter various hydrological conditions. Based on different water levels, values of 0.5 m, 1.55 m, 3.10 m, and 4.60 m are selected to represent the low water level, normal water level, high water level, and flood level, respectively. This study simulates the construction responses of the shield tunnel under the four river water levels using FLAC3D.

4.1. Impact on Pore Water Pressure

When groundwater is present, these changes affect the internal pore structure, leading to modifications in permeability characteristics across strata. Consequently, pore water redistributes to reach a new hydraulic equilibrium. The pore water pressure response is shown in Figure 4. The pore pressure field exhibits a stratified distribution pattern similar to that of the stress field, indirectly reflecting the interaction between the stress and seepage fields during tunnel excavation.

The disturbance caused by shield tunneling compromises the integrity of the soil structure, forming localized seepage channels and redistributing pore pressure. This leads to the formation of low-pressure zones around the tunnel, as indicated by the blue regions in the figure, which accelerate soil softening and exacerbate stratum instability. Under low water level conditions, the pore pressure distribution is shallow and concentrated near the tunnel face. At normal water level, the pressure gradient increases, forming a gradient zone centered on the tunnel. Under high and flood water level conditions, the pore pressure zone expands significantly, and values increase markedly—from a surface maximum of 405 kPa at low water level to 446 kPa at flood level. Particularly under flood conditions, pore pressure around the tunnel crown and side walls increases significantly, and the wide pressure diffusion zone may pose a threat to the safety of support structures. Overall, rising water levels intensify the influence of groundwater on soil strata, highlighting the need to consider structural instability caused by seepage.



(**a**) 0.5 m (**b**) 1.55 m

(**c**) 3.1 m (**d**) 4.6 m

Figure 4. Pore Water Pressure Contour Maps under Different Water Levels.

4.2. Influence of River Water Level on Stress

After long-term geological movements, the original strata, influenced by factors such as self-weight stress and water pressure, form an initial stress field. Under the working condition considering the seepage field, the presence of pore water pressure will reduce the effective stress field of the surrounding soil. Under the working condition considering the seepage field, the presence of pore water pressure will reduce the effective stress field of the surrounding soil. The calculation results of ground stress after excavation are shown in Figure 5. The stress field and the pore pressure field share a similar layered distribution pattern, which also indirectly reflects the mutual influence between the seepage field and the stress field during tunnel excavation. As the river water level rises, the range of high-stress zones (in red) around the tunnel increases significantly, and the vertical stress distribution in the strata changes markedly. Under low-water-level conditions, the stress changes at the top and around the tunnel are relatively moderate, with a small range and shallow concentration zones. At normal water level, a more pronounced stress concentration zone appears above the tunnel, indicating an enhanced impact of construction disturbance. Under high water and flood level conditions, the range of vertical stress expands further, and a high-stress core forms particularly near the tunnel crown. The stress around the tunnel increases gradually from 195 kPa at low water level to 205.3 kPa at flood level, indicating that water pressure has a significant effect on the stability of the surrounding soil [45]. Overall, the rise in water level makes the stress field of the strata more complex, and the stress concentration zone gradually extends upward, requiring reinforcement measures above the tunnel under high-water-level conditions [46–48].

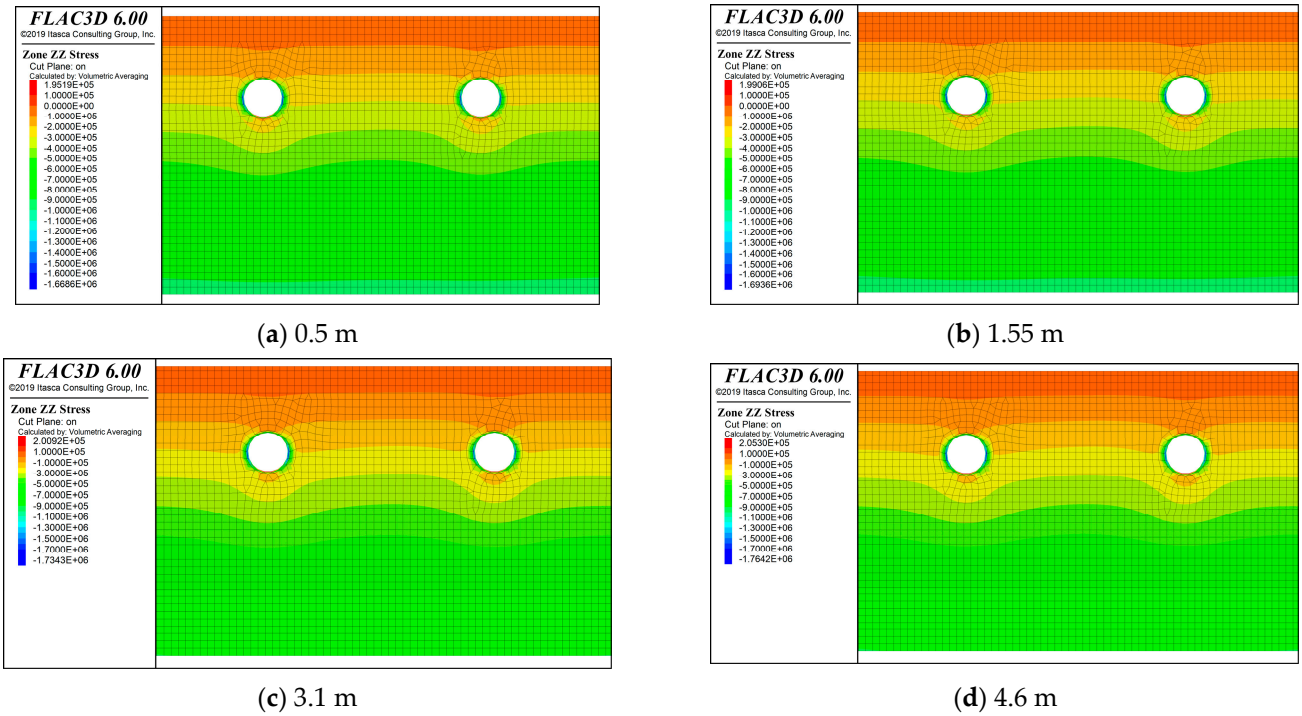


Figure 5. Vertical Stress Contour Maps under Different Water Levels.

4.3. Impact on Displacement

As the tunnel excavation progresses, both the stress and seepage fields in the stratum evolve toward a new equilibrium, resulting in varying degrees of deformation throughout the ground. The evolution of ground settlement with varying water levels is illustrated in Figure 6. The surface settlement profile exhibits a typical bell-shaped curve. After excavation is completed, the maximum settlement occurs directly above the tunnel. The maximum settlement and affected area above the left tunnel are significantly greater than those above the right tunnel. Both the width and depth of the settlement trough increase with rising water levels. Meanwhile, the upward displacement (heave) at the invert of the right tunnel exceeds that of the left. Both the magnitude and extent of this heave increase with higher water levels. Under low water level conditions, settlement is concentrated directly above the tunnel, with a maximum value of 7.63 mm. At flood water level, settlement increases significantly. The settlement influence zone expands from approximately one tunnel diameter under low water to about 2.5 times the diameter at high water, with a maximum settlement of 12.71 mm.

The horizontal displacement contours under different water levels, shown in Figure 7, reveal that displacement is mainly concentrated on both sides of the tunnel and exhibits only minor variation, indicating limited influence of tunneling disturbance on horizontal displacement. Directional differentiation of displacement is observed: the soil above the tunnel rises due to buoyancy, resulting in positive displacement, while the soil at the sidewalls is pushed inward by seepage forces, causing negative displacement [49–51].

Under low water level, horizontal displacement is minimal and roughly symmetrical, concentrated around the shield with limited extent, reflecting relatively high shear strength of the soil. As water level rises to the normal stage, the extent of horizontal displacement increases, and lateral deformation becomes more pronounced. Under high and flood water levels, large-scale lateral movement appears around the tunnel, particularly at the sides and invert, with increasing deformation trends. At flood stage, the maximum displacement reaches twice that observed at low water level, extending into the slopes on both riverbanks [52]. The greatest displacement occurs under flood conditions, indicating

that rising water levels not only affect vertical settlement but also intensify lateral sliding in the strata, imposing more stringent requirements on the deformation resistance of the tunnel structure [53–55].

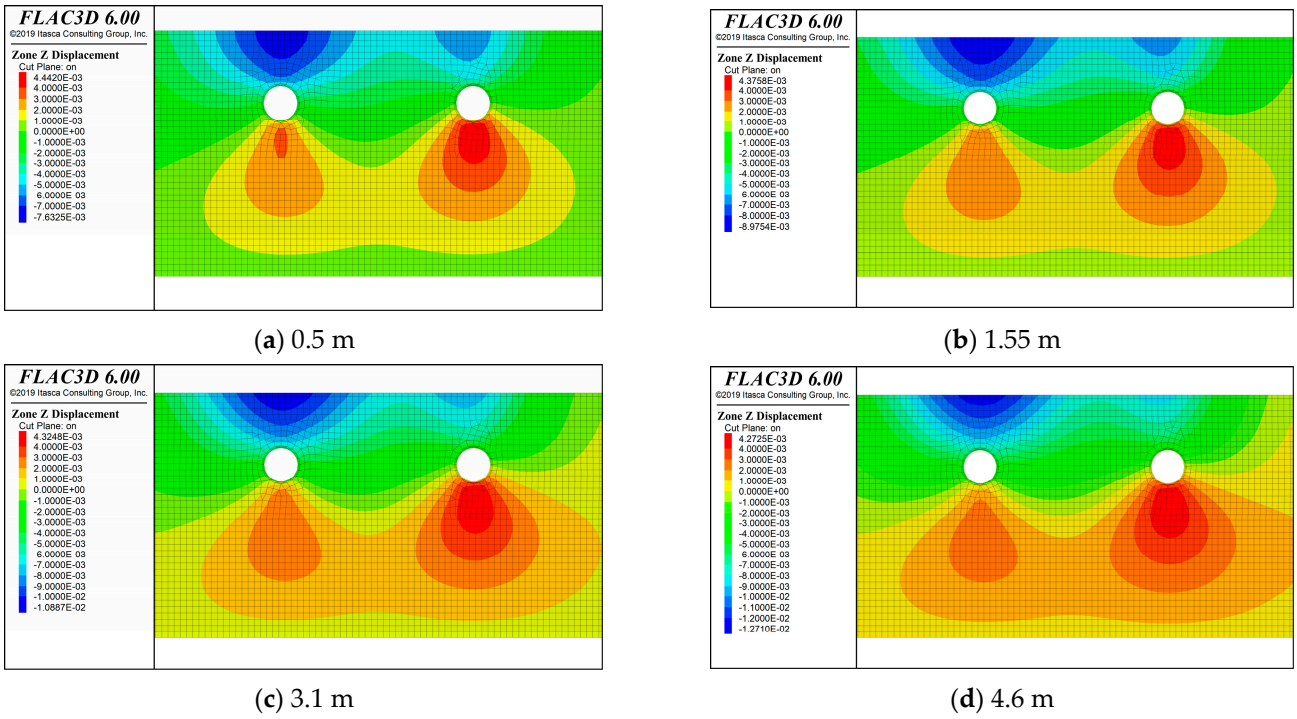


Figure 6. Vertical Settlement Contour Maps under Different Water Levels.

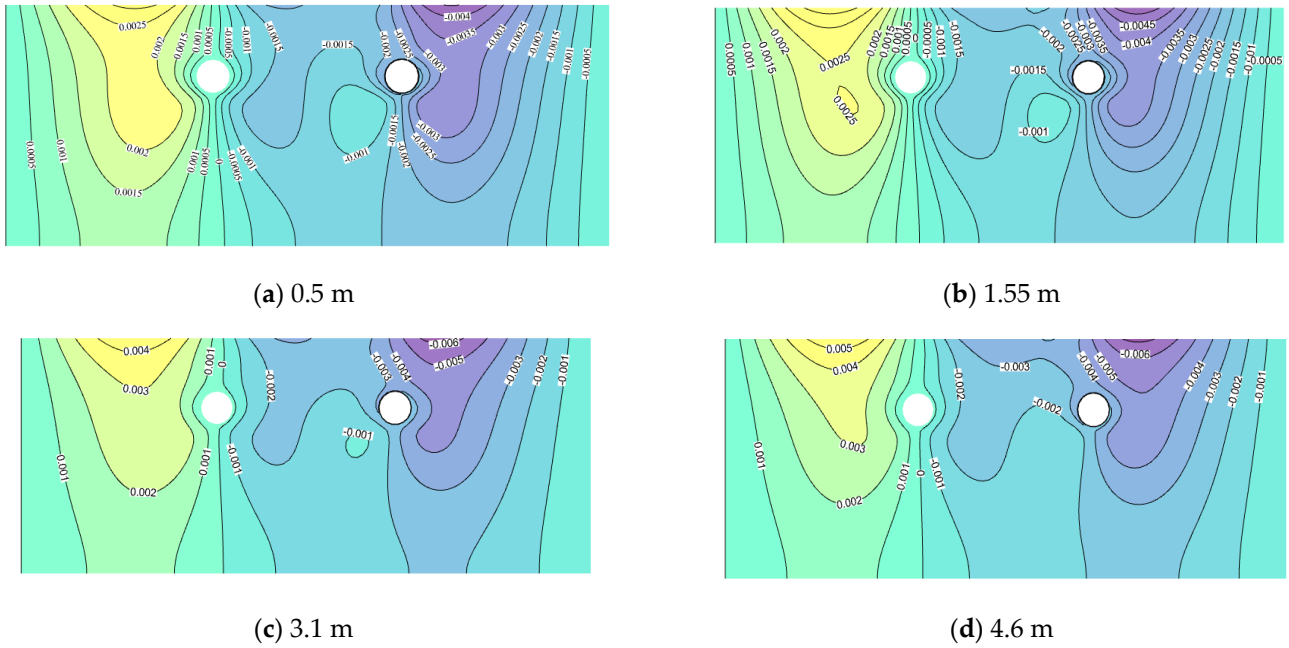


Figure 7. Contour plots of horizontal displacements at different water levels.

4.4. Impact on Ground and Tunnel Response

Figures 8 and 9 illustrate the variation in vertical surface displacement directly above the left and right tunnels at y = 50 m under different water level conditions. Prior to the arrival of the tunnel boring machine (TBM), the ground exhibits a slight heave of 1 to 2 mm due to the extrusion effect at the tunnel face. However, as the TBM advances, the soil begins to settle, and the magnitude of settlement gradually increases. By excavation step

90, settlement tends to stabilize and exhibits minimal further change. As water level rises, surface settlement increases progressively; for the left tunnel, the maximum settlement is 7.63 mm at low water level, 8.97 mm at normal level, 10.9 mm at high water, and 12.7 mm under flood conditions. The maximum settlement at flood level on the left side increases by 41.58% compared to the normal water level. For the right tunnel, the surface settlement increases from 6.54 mm at normal water level to 8.54 mm under flood conditions, a 30.6% rise. Although the overall trend of settlement for both tunnels is consistent, the right tunnel exhibits slightly smaller settlement.

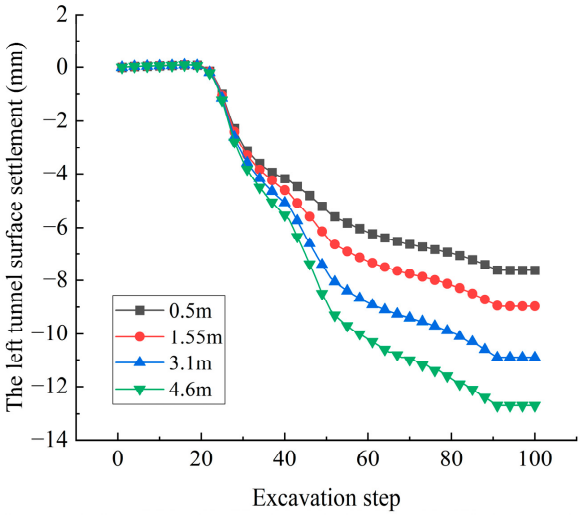


Figure 8. Vertical surface displacement above the left tunnel under different water levels.

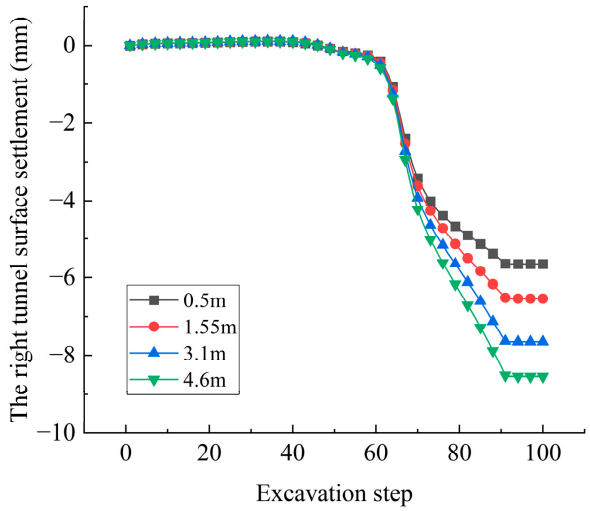


Figure 9. Vertical surface displacement above the right tunnel under different water levels.

As shown in Figure 10, the vertical displacement of the crown of the left tunnel under different water levels is presented. At excavation step 20, the crown experiences a sharp change in settlement, with an accelerated rate of displacement. As the water level rises, crown settlement increases progressively, with maximum values of 4.83 mm under low water level, 5.43 mm under normal water, 6.26 mm under high water, and 7.07 mm under flood level. The maximum settlement increases from 4.83 mm at low water level to 7.07 mm under flood conditions, representing a 46.37% increase.

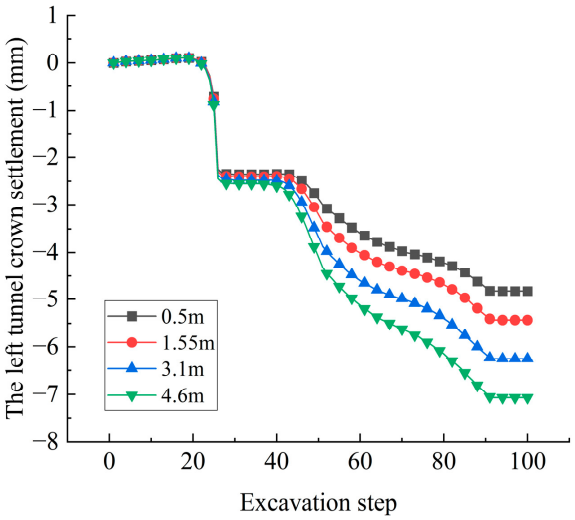


Figure 10. Vertical displacement at the crown of the left tunnel under different water levels.

Figure 11 shows the vertical displacement of the invert of the left tunnel under different water levels. Between excavation steps 25 and 35, the rate of uplift accelerates, reaching a peak at step 50. This phenomenon is attributed to increased groundwater pressure generating buoyant forces. However, as the TBM advances and stress at the excavation face is released, the soil beneath the tunnel undergoes instantaneous unloading, leading to elastic rebound under negative excess pore pressure, and the uplift gradually diminishes. The opposite deformation trends at the crown and invert suggest a bending-like response of the tunnel cross-section [56,57]. If this response is not properly controlled, it may increase the risk of lining cracking or joint opening, highlighting the need for enhanced monitoring and timely support measures during construction [58,59].

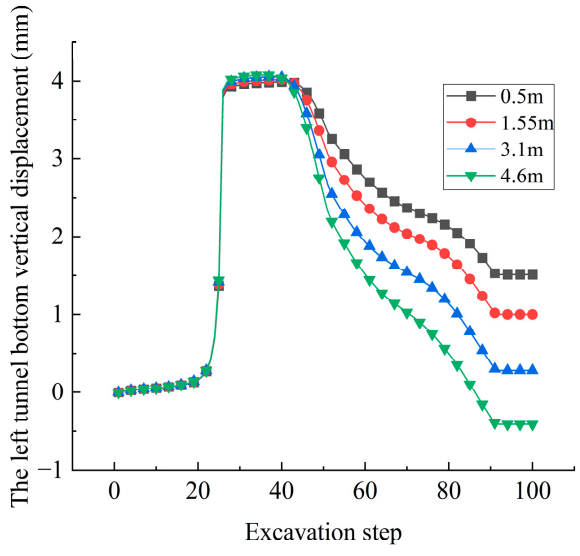


Figure 11. Vertical displacement at the invert of the left tunnel under different water levels.

4.5. Model Validation

To monitor the vertical displacement of the riverbank and riverbed surface during shield tunneling beneath the river, precision leveling instruments and other surveying tools were employed. In addition to riverbed monitoring, measurement points were installed on the riverbank crest and at the interface between the riverbank and the riverbed, as shown in Figure 12, which illustrates the layout of surface monitoring points for the

under-river construction section. The field monitoring data from transverse sections at y = 10 m, 50 m, and 90 m were compared with simulated settlement results, as shown in Figure 13, to examine their similarities and differences. All three sets of curves exhibit a Gaussian distribution pattern, with both measured and simulated maximum settlements concentrated near the centerline, consistent with the theory of surface settlement troughs induced by twin tunnels. The measured maximum settlements at y = 10 m, 50 m, and 90 m were 5.42 mm, 9.18 mm, and 7.23 mm, respectively, while the corresponding simulated values were 4.78 mm, 7.98 mm, and 6.37 mm. The corresponding error rates were 13.38%, 15.04%, and 13.50%, all of which fall within acceptable limits. The settlements obtained from numerical analysis are slightly smaller than the measured values, mainly because convergence was assumed once the maximum unbalanced force of the surrounding ground after excavation reached a relatively small value, without considering time-dependent effects, and because discrepancies between the adopted calculation parameters and actual ground properties are unavoidable.

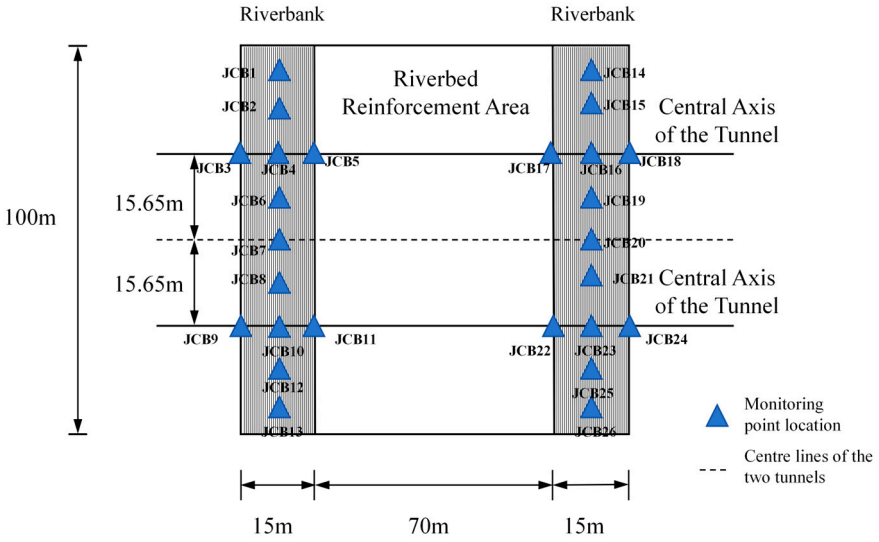


Figure 12. Plan Layout Diagram of Monitoring Points for Shield Tunnel Sections.

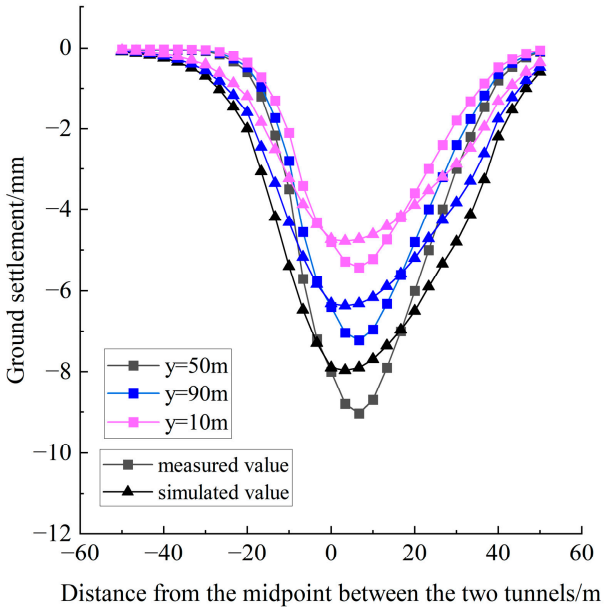


Figure 13. Comparison diagram of measured and computed ground settlement during excavation.

FLAC3D has developed specialized constitutive models for solving geotechnical engineering problems, offering more than ten selectable constitutive models. It is also equipped with the powerful built-in FISH language, which allows the definition of new variables or functions to meet special requirements, as well as robust pre- and post-processing capabilities that enable real-time analysis of results during computation. Using FLAC3D to simulate cross-river projects allows modeling of cross-river tunnel excavation under various scenarios and environments. It can systematically quantify key risks such as river dynamic water pressure, twin-tunnel proximity effects, and stratum seepage stability [60–62]. This provides a quantitative basis for optimizing support design parameters, comparing construction methods, and controlling environmental risks, thereby significantly enhancing the level of scientific decision-making for tunnel engineering under complex hydrogeological conditions [63–65].

4.6. Sensitivity Analysis

In the numerical model established using FLAC3D, the main physical and mechanical parameters involved in each soil layer include elastic modulus (E), Poisson's ratio (μ), cohesion (c), internal friction angle (φ) and so on. Performing inverse calculations for all parameters simultaneously incurs high computational costs and significant complexity. Therefore, it is necessary to conduct a sensitivity analysis of the various factors affecting surface deformation to identify the most sensitive ones and thereby determine the primary and secondary mechanical parameters. Sensitivity analysis evaluates parameters with varying degrees of sensitivity to ensure the reliability and accuracy of numerical simulations [66,67].

Sensitivity analysis is a fundamental method in the field of systems analysis. It assumes that a system consists of a system characteristic P and its n contributing factors, expressed as $P = f\ (x1, x2, x3, \ldots, xn)$. Starting from the baseline state $P^* = f\ (x1^*, x2^*, x3^*, \ldots, xn^*)$, each factor varies within its possible range to investigate and predict the impact of these variations on the system characteristic P. If a small change in xi results in a significant change in P, it indicates that P is sensitive to xi, and xi is considered a highly sensitive parameter of the system characteristic P; otherwise, it is regarded as a low-sensitivity parameter. To facilitate comparative analysis of sensitivity among different factors, it is necessary to normalize all factors in the system.

The sensitivity Sk is defined as follows [68,69]:

$$S_k = \frac{|\Delta P|}{P} / \frac{|\Delta x_k|}{\Delta x_k} = \left|\frac{\Delta P}{\Delta x_k}\right| \cdot \frac{P}{x_k},\ k = 1, 2, \cdots, n \tag{11}$$

When the value of $\frac{|\Delta x_k|}{\Delta x_k}$ is very small, S_k can be approximated as:

$$S_k = \left|\frac{d\Delta P}{d\Delta x_k}\right| \cdot \frac{P}{x_k},\ k = 1, 2, \cdots, n \tag{12}$$

where $\left|\frac{\Delta P}{P}\right|$ represents the relative variation rate of the system characteristic and $\left|\frac{\Delta x_k}{x_k}\right|$ represents the relative variation rate of a specific factor.

Based on the parameters set in the model and relevant engineering experience, pore water pressure, internal friction angle, and the elastic modulus of the supporting structure are identified as the primary influencing factors. Due to the extended construction period of tunnel excavation, the flow of Zhanqiao Port is susceptible to variations caused by weather conditions. During the flood season, the maximum flood level of the Zhanqiao Port waterway can reach 4.60 m, while the normal water level is 1.55 m. In addition, practical metro tunnel design must consider the variability of the soil's internal friction angle and tailor the design of the supporting structure according to geological conditions

to optimize economic efficiency. Based on these influencing factors, extensive numerical simulations of tunnel excavation were conducted under varying pore water pressures, internal friction angles, and elastic moduli of supporting structures to understand soil settlement resulting from changes in key factors. A single-factor control method was adopted for the design, with the specific computational schemes presented in Table 2.

Table 2. Sensitivity analysis scheme of shield tunneling parameters.

Simulation Case ID	Pore-Pressure ($\times 10^4$ Pa)	Friction Angle (°)	Elastic Modulus (GPa)
1	40.50	13.2	18.5
2	41.55	13.2	18.5
3	43.10	13.2	18.5
4	44.60	13.2	18.5
5	41.55	8.0	18.5
6	41.55	14.7	18.5
7	41.55	16.6	18.5
8	41.55	13.2	10.5
9	41.55	13.2	26.5
10	41.55	13.2	34.5

Relationship Between Displacement and Different Factors

Figure 14 illustrates the approximately linear relationship between pore water pressure and the vertical displacement of the tunnel-surrounding soil. Simulation results show that as pore pressure increases, the vertical displacement also increases nearly proportionally. This indicates that higher pore pressure reduces soil strength and promotes ground deformation, highlighting the critical influence of pore pressure on tunnel stability. The relationship between displacement and internal friction angle is illustrated in Figure 15. As the internal friction angle increases, the vertical displacement shows an approximately linear decrease. When the internal friction angle increases from 8° to 16.6°, the vertical displacement of the tunnel-surrounding soil decreases from 10.39 mm to 9.745 mm. The relationship between displacement and the elastic modulus of the supporting structure is illustrated in Figure 16. As the elastic modulus of the supporting structure increases, vertical displacement decreases in an approximately linear manner. When the elastic modulus of the supporting structure increases from 10.5 GPa to 34.5 GPa, the vertical displacement of the surrounding soil decreases from 14.2 mm to 3 mm.

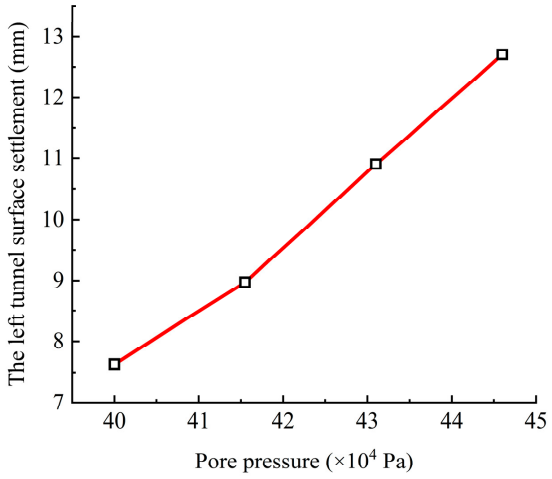


Figure 14. Pore Water Pressure.

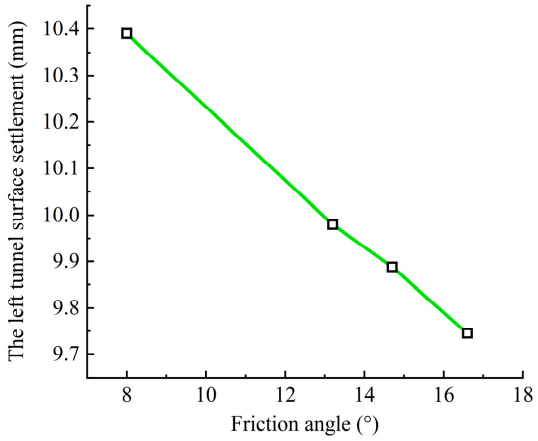


Figure 15. Internal Friction Angle.

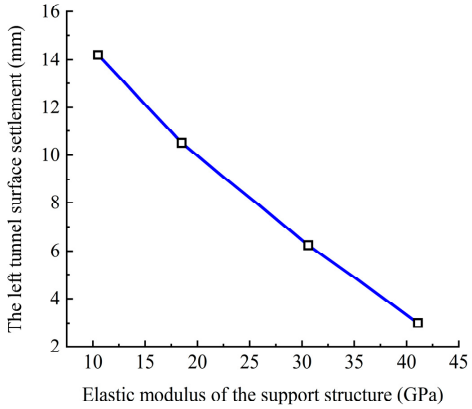


Figure 16. Elastic Modulus of Supporting Structures.

An orthogonal experimental design is adopted to investigate the sensitivity response mechanism of ground surface settlement under multi-factor coupling effects. Pore-pressure, elastic modulus of the supporting structure, internal friction angle, tunnel spacing, and tunnel burial depth are selected as the influencing factors for the multi-factor sensitivity analysis, aiming to quantitatively reveal the contribution and interaction effects of each parameter on ground surface settlement and to provide guidance for subsequent design and construction, as shown in Table 3.

Table 3. Influencing factors and levels in the orthogonal experiment.

Parameter	Level 1	Level 2	Level 3	Level 4
Pore-pressure ($\times 10^4$ Pa)	40.50	41.55	43.10	44.60
Elastic Modulus (GPa)	10.5	18.5	26.5	34.5
Friction Angle (°)	8.0	13.2	14.7	16.6
Tunnel Spacing	10	17	24	31.29
Tunnel Depth	6	8.73	11	13

As indicated in the above Table 4, five parameters influencing the orthogonal experiment were considered, each with four levels and based on the selected parameters and levels, and an L16 (45) orthogonal array was adopted, as shown in Table 4, to design 16 experimental cases, thereby systematically evaluating the sensitivity of ground

surface settlement to each parameter and providing a scientific basis for optimizing shield tunneling construction.

Table 4. Experimental scheme table.

Simulation Case ID	Level Combination	Pore-Pressure ($\times 10^4$ Pa)	Elastic Modulus (GPa)	Friction Angle (°)	Tunnel Spacing	Tunnel Depth	Experimental Value
1	$A_1B_1C_1D_1E_1$	40.50	10.5	8.0	10	6	X_1
2	$A_1B_2C_2D_2E_2$	40.50	18.5	13.2	17	8.73	X_2
3	$A_1B_3C_3D_3E_3$	40.50	26.5	14.7	24	11	X_3
4	$A_1B_4C_4D_4E_4$	40.50	34.5	16.6	31.29	13	X_4
5	$A_2B_1C_2D_3E_4$	41.55	10.5	8.0	24	13	X_5
6	$A_2B_2C_1D_4E_3$	41.55	18.5	13.2	31.29	11	X_6
7	$A_2B_3C_4D_1E_2$	41.55	26.5	14.7	10	8.73	X_7
8	$A_2B_4C_3D_2E_1$	41.55	34.5	16.6	17	6	X_8
9	$A_3B_1C_3D_4E_2$	43.10	10.5	8.0	31.29	8.73	X_9
10	$A_3B_2C_4D_3E_1$	43.10	18.5	13.2	24	6	X_{10}
11	$A_3B_3C_1D_2E_4$	43.10	26.5	14.7	17	13	X_{11}
12	$A_3B_4C_2D_1E_3$	43.10	34.5	16.6	10	11	X_{12}
13	$A_4B_1C_4D_2E_3$	44.60	10.5	8.0	17	11	X_{13}
14	$A_4B_2C_3D_1E_4$	44.60	18.5	13.2	10	13	X_{14}
15	$A_4B_3C_2D_4E_1$	44.60	26.5	14.7	31.29	6	X_{15}
16	$A_4B_4C_1D_3E_2$	44.60	34.5	16.6	24	8.73	X_{16}

Numerical simulations were conducted to establish the 16 models defined in the above scheme, with maximum ground surface settlement taken as the output indicator, in order to investigate the influence of pore water pressure, elastic modulus of the supporting structure, internal friction angle, tunnel spacing, and tunnel burial depth on shield excavation-induced ground settlement. Range analysis was employed to evaluate the sensitivity of ground surface settlement to each influencing factor. Specifically, the mean values of the experimental results at each level of every factor were first calculated, followed by the determination of the range of these mean values. By computing the average settlement at different levels of each factor and determining the corresponding range (R), the relative influence of each factor on settlement can be assessed. The maximum ground surface settlement values obtained from the 16 models were denoted as X_1~X_{16}.

As shown in Table 5, the influencing factors affecting ground surface settlement, ranked from most to least significant, are $R_A > R_C > R_B > R_E > R_D$, corresponding to pore water pressure, internal friction angle, elastic modulus of the supporting structure, tunnel burial depth, and tunnel spacing, respectively. In saturated soft soil conditions, pore water pressure exhibits the highest sensitivity, with a value of 13.19, indicating its dominant influence on ground surface deformation. Following pore water pressure, the internal friction angle shows relatively high sensitivity, whereas tunnel spacing is the least sensitive factor.

Table 5. Table of Maximum Ground Surface Settlement and Range.

Experiment ID	X_1	X_2	X_3	X_4	X_5	X_6	X_7	X_8
Test result (mm)	29.91	26.58	23.47	20.32	27.84	24.96	22.05	18.94
Experiment ID	X_9	X_{10}	X_{11}	X_{12}	X_{13}	X_{14}	X_{15}	X_{16}
Test result (mm)	23.12	20.41	17.66	14.83	18.52	15.87	11.26	1.88
Range index	R_A	R_B	R_C	R_D	R_E			
Range	13.19	5.89	8.37	0.49	1.76			

5. Discussion

(1) Under-river crossing is one of the most high-risk critical procedures in shield tunneling, and variations in river water level have a significant influence on excavation face stability and lining stress conditions. Based on the geological and hydrological conditions of the project, staged construction parameter recommendations corresponding to different water levels are proposed. Based on the geological and hydrological conditions of the project, staged construction parameter recommendations corresponding to different water levels are proposed. During the low-water stage, reduced overlying hydraulic load and low total ground stress require construction control to focus on preventing riverbed heave or slurry blowout caused by excessive chamber pressure, and a low-pressure equilibrium principle should be adopted, with chamber pressure controlled at the lower bound of calculated values, synchronous grouting pressure slightly higher than hydrostatic pressure, and enhanced shield attitude monitoring, with a recommended face pressure of 0.255 MPa. The normal-water stage features relatively stable conditions and represents a critical period for establishing baseline excavation parameters, during which the matching relationships among advance rate, cutterhead rotation speed, and torque should be calibrated through trial sections, with a recommended face pressure of 0.270 MPa. During the high-water stage, hydraulic head pressure increases markedly and groundwater readily infiltrates the excavation system, shifting construction risks toward blowout and structural uplift, thereby necessitating enhanced muck conditioning and increased tail-seal and grouting capacity to form an effective waterproofing system, with a recommended face pressure of 0.295 MPa. Under flood-level conditions, riverbed scour and extreme hydraulic head pressure may significantly reduce construction safety margins, and the face pressure should be increased to 0.320 MPa.

(2) In silty clay with low cohesion, low modulus, and high compressibility, the proportion of effective stress is inherently low. A rise in groundwater level increases pore water pressure, significantly reducing effective stress and shear strength, which makes the soil prone to plastic deformation and settlement. High groundwater levels weaken the soil arching effect above the tunnel crown and may induce uplift at the arch foot. Although shield tunneling can cause partial rebound, consolidation settlement generally dominates, leading to invert subsidence.

(3) Due to differences in excavation and support methods, as well as variations in engineering geology, different twin-tunnel responses occur in each project. In this project, the settlement of the left tunnel is greater than that of the right tunnel, which is related to the larger spacing between the two lines and the shorter construction interval. the left tunnel experienced greater settlement due to concentrated stress release during its first excavation, which formed a larger plastic zone and caused early-stage settlement that was difficult to recover. The right tunnel, excavated later, exhibited a wider inverted uplift range due to reduced lateral confinement from prior disturbances.

6. Conclusions

This study establishes a three-dimensional numerical model to analyze stress distribution, pore water pressure, and ground settlement under different water levels. The simulation results are validated using field monitoring data, and a sensitivity analysis identifies the key factors controlling soil settlement. The main conclusions are as follows.

(1) Taking the water-rich sandy strata of the Longteng Street Station to Zhangjiaqiao Road Station section of Hangzhou Metro Line 15 in China as the engineering background, the patterns of ground settlement and pore pressure changes following shield tunneling were numerically simulated. Through a comparative analysis between the numerical simulation results and field measurements of ground settlement, the simulated data were

found to be in good agreement with the observed results, exhibiting consistent settlement patterns and trends. This consistency validates the accuracy and rationality of the three-dimensional fluid–solid coupling simulation model, the computational methodology, and the selection of mechanical parameters.

(2) Based on the saturated soft soil conditions prevalent in China's coastal regions, the dynamic process of soil settlement induced by the interaction of pore water pressure and stress via fluid–solid coupling was systematically investigated under four water level scenarios: low, normal, high, and flood levels. The research results indicate that water level variations exert a significant influence on vertical ground displacement, with surface settlement exhibiting a marked increasing trend as the water level rises. Consequently, during shield tunneling beneath rivers, the tunnel face support pressure should be dynamically adjusted in accordance with real-time water levels. This study establishes a reference range for tunnel face pressure tailored to various water level scenarios, providing engineering guidance for shield tunneling beneath rivers in coastal saturated soft ground.

(3) Utilizing orthogonal experimental design and range analysis, the influence degrees of five factors—pore water pressure, internal friction angle, elastic modulus of the support structure, tunnel burial depth, and tunnel spacing—on ground settlement were quantitatively evaluated. The results demonstrate that in saturated soft soil regions, pore water pressure exhibits the highest sensitivity to ground settlement and serves as the primary controlling factor for surface deformation. The internal friction angle follows in sensitivity, whereas tunnel spacing has the least significant impact on ground settlement. These research findings provide a scientific basis and reference for safety control and stability assessment during the construction of shield tunnels.

Author Contributions: Conceptualization and writing—original draft preparation, J.T.; investigation, Z.R. and X.D. All authors have read and agreed to the published version of the manuscript.

Funding: This study received backing from the Zhejiang Province Public Interest Technology Research Programme Project of China (Grant No. LGF21E090005).

Data Availability Statement: Data supporting this study are available from the corresponding author upon reasonable request.

Conflicts of Interest: The authors declare no conflicts of interest.

References

1. Zhang, H.; Lv, Y.; Guo, J. New development direction of underground logistics from the perspective of public transport: A systematic review based on scientometrics. *Sustainability* **2022**, *14*, 3179. [CrossRef]
2. Wu, G.; Tan, Y.; Zeng, J.; Zheng, J.; Zhang, R.; Liu, Y.; Yue, S. Laboratory tests of an eccentrically loaded strip footing above single underlying void. *J. Build. Eng.* **2025**, *111*, 113211. [CrossRef]
3. Tong, L.; Fu, L.; Wu, B.; Xu, C.; Lim, C.W. Packing fraction effect on dynamic creep deformation of granular materials. *Acta Geotech.* **2025**, *20*, 2135–2144. [CrossRef]
4. Tong, L.; Fu, L.; Wu, B.; Xu, C.; Lim, C.W.; Ding, H. Particle Shape Effect on Creep and Fluidity of Granular Packing. *J. Eng. Mech.* **2025**, *151*, 8435. [CrossRef]
5. Wang, Z.; Dong, J.; Zhao, Y.; Wang, Z. Analysis of Fluid–Structure Coupling of Sudden Water Deformation in Tunnels Under Construction. *Water* **2024**, *16*, 3479. [CrossRef]
6. Zhang, S.; Cheng, X.; Li, X.; Qi, L. Liquid-Solid Coupling Response of Surrounding Rock Mass of Large-Diameter River-Crossing Shield Tunnel. *Civ. Eng. J.-Staveb. Obz.* **2023**, *32*, 443–456. [CrossRef]
7. Luo, B.; Su, Y.; Ding, X.; Chen, Y.; Liu, C. Modulation of initial CaO/Al_2O_3 and SiO_2/Al_2O_3 ratios on the properties of slag/fly ash-based geopolymer stabilized clay: Synergistic effects and stabilization mechanism. *Mater. Today Commun.* **2025**, *47*, 113295. [CrossRef]
8. Luo, B.; Su, Y.; Hu, X.; Chen, Z.; Chen, Y.; Ding, X. Strength behavior and microscopic mechanisms of geopolymer-stabilized waste clays considering clay mineralogy. *J. Clean. Prod.* **2025**, *530*, 146877. [CrossRef]

9. Su, Y.; Luo, B.; Luo, Z.; Xu, F.; Huang, H.; Long, Z.; Shen, C. Mechanical characteristics and solidification mechanism of slag/fly ash-based geopolymer and cement solidified organic clay: A comparative study. *J. Build. Eng.* **2023**, *71*, 106459. [CrossRef]
10. Ding, H.; Yu, Y.; Xu, C.; Pu, X.; Guo, W.; Tong, L. Analytical modeling for nonlinear seismic metasurfaces of saturated porous media. *Int. J. Mech. Sci.* **2025**, *303*, 110666. [CrossRef]
11. Shi, Y.; Wang, Y.; Wang, L.-N.; Wang, W.-N.; Yang, T.-Y. Bridge Tower Warning Method Based on Improved Multi-Rate Fusion Under Strong Wind Action. *Buildings* **2025**, *15*, 2733. [CrossRef]
12. Shi, Y.; Wang, Y.; Wang, L.-N.; Wang, W.-N.; Yang, T.-Y. Bridge Cable Performance Warning Method Based on Temperature and Displacement Monitoring Data. *Buildings* **2025**, *15*, 2342. [CrossRef]
13. Wang, L.; Zhang, J.-G.; Sha, H.-Y.; Wang, Y.-R.; Wang, H.-Y.; Zhu, G.-C.; Lu, Y.-Z. Lanthanum-quaternized chitosan-modified zeolite for long-lasting operation of constructed wetland: A bifunctional strategy for simultaneous phosphorus removal and microbial clogging mitigation. *Water Res.* **2025**, *288*, 124688. [CrossRef] [PubMed]
14. Yu, N.; Zeng, X.; Ma, X.; Sun, Y.; Wang, Y.; Chen, B.; Luo, Z.; Dong, C.; Shen, K.; Wu, J. Preparation of Ce-Fe_2O_3/Al_2O_3 catalyst for simultaneous degradation of benzodiacetone and reduction of Cr(VI) by electro-Fenton process: Performance, mechanism, degradation pathways. *J. Alloys Compd.* **2025**, *1045*, 184745. [CrossRef]
15. Zeng, S.; Tao, Y.; Sun, H.; Wang, Y. Semi-supervised ensemble model for TBM rock mass classification. *Tunn. Undergr. Space Technol.* **2025**, *162*, 106632. [CrossRef]
16. Islam, M.S.; Iskander, M. Three-dimensional numerical investigation of ground settlement caused by piggyback twin tunnels. *Tunn. Undergr. Space Technol.* **2023**, *134*, 104970. [CrossRef]
17. Hao, D.; Zhu, R.; Wu, K.; Chen, R. Analysis of Ground Settlement Caused by Double-line TBM Tunnelling Under Existing Building. *Geotech. Geol. Eng.* **2021**, *40*, 899–911. [CrossRef]
18. Huang, J.; Xu, P.; Huang, Z. Settlement Analysis of Mud-Water Shield Passing Full-Face Water-Rich Sand and Cobble Stratum Under Luo River. *Geotech. Geol. Eng.* **2023**, *42*, 535–542. [CrossRef]
19. Liu, J.; Yang, Y.; Yang, C. Analysis and Prediction of Long-Term Settlement of Metro Shield Tunnel in Saturated Sand. *Geotech. Geol. Eng.* **2021**, *39*, 5241–5252. [CrossRef]
20. Ma, Y.; Yang, J.; Li, L.; Li, Y. Analysis on ultimate water pressure and treatment measures of tunnels operating in water rich areas based on water hazard investigation. *Alex. Eng. J.* **2022**, *61*, 6581–6589. [CrossRef]
21. Huang, S.; Lyu, Y.; Sha, H.; Xiu, L. Seismic performance assessment of unsaturated soil slope in different groundwater levels. *Landslides* **2021**, *18*, 2813–2833. [CrossRef]
22. Pagnozzi, M.; Coletta, G.; Leone, G.; Catani, V.; Esposito, L.; Fiorillo, F. A steady-state model to simulate groundwater flow in unconfined aquifer. *Appl. Sci.* **2020**, *10*, 2708. [CrossRef]
23. Schwartz, F.W.; Zhang, H. *Fundamentals of Groundwater*; John Wiley & Sons: Hoboken, NJ, USA, 2024.
24. Zhang, E.; Meng, C.; Qu, J.; Zhu, Z.; Niu, J.; Wang, L.; Song, N.; Yin, Z. Dual effects of Caragana korshinskii introduction on herbaceous vegetation in Chinese desert areas: Short-term degradation and long-term recovery. *Plant Soil* **2025**, *508*, 145–162. [CrossRef]
25. Sun, Y.; Liu, J.; Chen, J.; Li, G.; Liang, M.; Zhang, M. Soft/Hard Interface Design of Bismuth Nanodots Embedded in $Ti_3C_2T_x$ Mxene for Highly Efficient Dechlorination Battery Deionization. *SSRN Electron. J.* **2025**, *614*, 119183. [CrossRef]
26. Wang, Y.; Li, F.; Li, Y.; Li, J.; Chen, H.; Bai, Y. Effects of ultrasonic surface rolling process on microstructure and mechanical properties of metastable $Fe_{50}Mn_{30}Co_{10}Cr_{10}$ high-entropy alloy fabricated by laser directed energy deposition. *J. Mater. Res. Technol.* **2025**, *39*, 26–46. [CrossRef]
27. Guo, Z.; Xu, L.; Zheng, Y.; Xie, J.; Wang, T. Bearing fault diagnostic framework under unknown working conditions based on condition-guided diffusion model. *Measurement* **2024**, *242*, 115951. [CrossRef]
28. Ji, X.; Yang, C. A coupled calculation model for rock mass structure and rock masses. *Rock Soil Mech.* **2006**, *25*, 763–768.
29. Li, J.; Liu, Y.; Li, H.; Cui, N.; Yu, K. A Unified Family of High-Order Energy-Conserving Time Integrators for Nonlinear Dynamical Problems. *Int. J. Numer. Methods Eng.* **2026**, *127*, e70253. [CrossRef]
30. Chen, X.-x.; Luo, Z.-j.; Zhou, S.-l. Influences of soil hydraulic and mechanical parameters on land subsidence and ground fissures caused by groundwater exploitation. *J. Hydrodyn.* **2014**, *26*, 155–164. [CrossRef]
31. Artamonova, N.; Sheshenin, S.; Frolova, Y.V.; Bessonova, O.Y.; Novikov, P. Calculating components of the effective tensors of elastic moduli and Biot's parameter of porous geocomposites. *Mech. Compos. Mater.* **2020**, *55*, 715–726. [CrossRef]
32. Whitaker, S. Flow in porous media I: A theoretical derivation of Darcy's law. *Transp. Porous Media* **1986**, *1*, 3–25. [CrossRef]
33. Selvadurai, A.; Suvorov, A. The influence of the pore shape on the bulk modulus and the Biot coefficient of fluid-saturated porous rocks. *Sci. Rep.* **2020**, *10*, 18959. [CrossRef] [PubMed]
34. Peck, R.B. Advantages and limitations of the observational method in applied soil mechanics. *Geotechnique* **1969**, *19*, 171–187. [CrossRef]
35. Fang, Q.; Tai, Q.; Zhang, D.; Wong, L.N.Y. Ground surface settlements due to construction of closely-spaced twin tunnels with different geometric arrangements. *Tunn. Undergr. Space Technol.* **2016**, *51*, 144–151. [CrossRef]

36. Li, Y.; Xie, K.; Zhou, J.; Kong, X. *Geotechnical Aspects of Underground Construction in Soft Ground*; CRC Press: Boca Raton, FL, USA, 2008; pp. 169–174.
37. Robert, D. A modified Mohr-Coulomb model to simulate the behavior of pipelines in unsaturated soils. *Comput. Geotech.* **2017**, *91*, 146–160. [CrossRef]
38. Li, Y.; Bian, X.; Peng, H.; Zhu, B.; Zhou, Y. Additional stress of soil and surface settlement during tunnel shield construction. *Buildings* **2023**, *13*, 1437. [CrossRef]
39. Zhao, B.; Lei, H.; Cheng, X.; Zheng, G. A hybrid machine learning algorithm for predicting excess pore water pressure caused by shield tunnelling in water rich silt layers. *Tunn. Undergr. Space Technol.* **2025**, *165*, 106898. [CrossRef]
40. Xu, P.; Chen, C.; Zhang, A. Research on Construction Technology and Formation Deformation of Shield Tunneling Under River. *Geotech. Geol. Eng.* **2021**, *39*, 3627–3638. [CrossRef]
41. Luo, Z.-j.; Zeng, F. Finite element numerical simulation of land subsidence and groundwater exploitation based on visco-elasticplastic biot's consolidation theory. *J. Hydrodyn.* **2011**, *23*, 615–624. [CrossRef]
42. Liu, J.; Guo, Z.; Wu, X.; Ren, Y.; Hu, M.; Zeng, H. Real-Time Observation of Breathing Vortex Solitons in a Yb:CALGO Laser. *Laser Photon-Rev.* **2025**, *20*, e01758. [CrossRef]
43. Yin, Z.; Chen, Y.; She, P.; Liu, C.; He, X.; Lv, S. Modeling the measurement precision of a multi-camera system. *Opt. Lett.* **2025**, *50*, 6489–6492. [CrossRef] [PubMed]
44. Liu, J.; Guo, Z.; Hu, M.; Zeng, H. Sub-100 Fs Vortex Beams Generated from a Yb:CALGO Laser. *Laser Photon-Rev.* **2025**, *19*, e00819. [CrossRef]
45. Cui, Y.; Chen, S.; Li, L.; Wang, X.; Liu, J. Atomistic insights into the hydration behavior of N-A-S-H Gel via Ca^{2+} substitution: A molecular dynamics simulation study. *J. Non-Cryst. Solids* **2025**, *673*, 123892. [CrossRef]
46. Liu, Z.; Qi, X.; Ke, J.; Shui, Z. Enhancing the toughness of ultra-high performance concrete through improved fiber-matrix interface bonding. *Constr. Build. Mater.* **2025**, *491*, 142616. [CrossRef]
47. Li, Z. Toward Low-Carbon Construction: A Review of Red Mud Utilization in Cementitious Materials and Geopolymers for Sustainability and Cost Benefits. *Buildings* **2026**, *16*, 362. [CrossRef]
48. Li, Z.; Gao, X.; Lu, D.; Dong, J. Early hydration properties and reaction kinetics of multi-composite cement pastes with supplementary cementitious materials (SCMs). *Thermochim. Acta* **2022**, *709*, 179157. [CrossRef]
49. Hu, W.; Cheng, W.-C.; Huang, Q.; He, P. Enhancement mechanism of electrokinetic remediation of a Cu- and Pb-contaminated loess by constructing a multi-electrode configuration. *Chem. Eng. J.* **2025**, *521*, 166880. [CrossRef]
50. Xu, D.-M.; Hu, X.-X.; Wang, W.-C.; Wang, J.; Shi, C.-C.; Zang, H.-F. Innovative daily runoff prediction model integrating black-winged kite algorithm and Mamba2–Transformer architecture. *Ecol. Inform.* **2025**, *93*, 103565. [CrossRef]
51. Zhang, Y.; Guo, X.; Wu, Y.; Zhang, Y.; Lü, C. Active control of cables with piezoelectric actuation considering geometric and material nonlinearities. *Eng. Struct.* **2025**, *340*, 120773. [CrossRef]
52. Fu, H.; Tian, J.; Chen, S.; Chin, C.-L.; Ma, C.-K. Axial compressive performance of CFRP-steel composite tube confined seawater sea-sand concrete intermediate slender columns. *Constr. Build. Mater.* **2024**, *441*, 137399. [CrossRef]
53. Wu, X.; He, J.; Tian, J.; Zheng, Y.; Fu, H.; Yuan, J.; Lu, S.; Huang, W. Degradation behaviors and damage model of the interface between ECC and concrete under sulfate wet-dry cycling. *Constr. Build. Mater.* **2025**, *476*, 141283. [CrossRef]
54. Fu, H.; Tian, J.; Chin, C.-L.; Liu, H.; Yuan, J.; Tang, S.; Mai, R.; Wu, X. Axial compression behavior of GFRP-steel composite tube confined seawater sea-sand concrete intermediate long columns. *Eng. Struct.* **2025**, *333*, 120157. [CrossRef]
55. Liu, H.; Chen, J.; Zhang, P.; Li, W.; Su, W.; Su, T.; Gong, S.; Li, B. Freeze-Thaw Behavior and Damage Prediction of Mixed Recycled Coarse Aggregate Concrete. *Buildings* **2026**, *16*, 368. [CrossRef]
56. He, Q.; Qu, C. Modular Landfill Remediation for AI Grid Resilience. *arXiv* **2025**, arXiv:2512.19202. [CrossRef]
57. Fan, D.; Liu, M.; Shao, Y.; Yang, L.; Liu, Y.; Zhang, Y.; Ren, Y.; Wang, Z. Domain-Specific Large Language Model for Maintenance Decision-Making on Wind Farms by Labeled-Data-Supervised Fine-Tuning. *Engineering* 2025, *in press*. [CrossRef]
58. Guo, Z.; Li, J.; Wang, T.; Xie, J.; Yang, J.; Niu, B. Dynamically Constrained Digital Twin-Based Mechanical Diagnosis Framework Under Undetermined States Without Fault Data. *IEEE Trans. Instrum. Meas.* **2025**, *74*, 3547715. [CrossRef]
59. Zhao, Y.; Ta, Y.; Bi, R.; Tang, B.; Lu, Z.; Yan, Y.; Xie, J.; Guo, Z. A cross-working-condition prediction method for bearing remaining useful life based on SPW-SVDD health indicators and temporal-self-attention mechanism. *Adv. Eng. Inform.* **2026**, *71*, 104313.
60. Gan, X.; Chen, Z.; Ma, W.; Zhang, Y.; Qu, J.; Han, C.; Li, Z. Kinetic and thermodynamic analyses of multigranular low-rank coal: Synergistic effect of particle size on reactivity and coke properties. *Fuel* **2025**, *406*, 137065. [CrossRef]
61. Gan, X.; Chen, Z.; Ma, W.; Zhang, Y.; Qu, J. Research on carbon structure evolution, surface chemical properties, microstructure, and mechanism of low-rank coal pyrolysis under different atmospheres. *J. Anal. Appl. Pyrolysis.* **2026**, *195*, 107607. [CrossRef]
62. Wan, Y.; Jing, T.; Ma, S.; Shen, F.; Liu, X. Ultra-wide microwave absorption with thin thickness in multi-layered Fe_3O_4-coated FeSiCr composites. *Appl. Surf. Sci.* **2025**, *687*, 162303. [CrossRef]

63. Tian, J.; Zhang, S.; Wu, X.; Zheng, Y.; Yu, W.; Wang, W.-W.; Yuan, J.; Fu, H.; Pang, S.; Zuo, Y. Study on the comprehensive performances of self-sensing ECC under coupling effect of temperature and load: Microscopic characterization, self-sensing performance, damage self-sensing theoretical model. *Constr. Build. Mater.* **2025**, *499*, 144088. [CrossRef]
64. Wu, X.; He, J.; Tian, J.; Liu, M.; Zheng, Y.; Zhang, W.; Yuan, J.; Wang, W.-W.; Fu, H.; Wang, R. Multi-scale performance of underwater-castable ultra-high-volume fly-ash eco-friendly engineered cementitious composites: Microstructural characterization, workability, mechanical properties and environmental effects. *Constr. Build. Mater.* **2025**, *506*, 144870. [CrossRef]
65. Wu, X.; Ouyang, X.; Tian, J.; Zheng, Y.; Fu, H.; Yuan, J.; Wang, W.-W.; Zuo, Y. Experimental study on mechanical and self-sensing properties of intelligence-function cement-based composite beams under marine erosion environment. *Structures* **2025**, *76*, 108950. [CrossRef]
66. Huang, J.; Zong, Z.; Wang, P.; Zhang, Y.; Diab, M.; Li, Z. N/P dual-doped niobium carbide MXene enhances ion transport kinetics for high-performance sodium-ion batteries. *J. Alloys Compd.* **2026**, *1051*, 185966. [CrossRef]
67. Huang, J.; Zong, Z.; Wang, P.; Zhou, H.; Zhang, Y.; Li, Z. Atomic-level steering of charge flow from type-II to S-scheme in In_2O_3/BiOCl via vacancy–metal pairs for CO_2 photoreduction. *Chem. Eng. J.* **2026**, *528*, 172537. [CrossRef]
68. Zheng, F.; Jiang, A.; Guo, X.; Min, Q.; Yin, Q. Back analysis of surrounding rock parameters of large-span arch cover station based on GP-DE algorithm. *Appl. Sci.* **2022**, *12*, 12590. [CrossRef]
69. Li, J.; Sun, W.; Su, G.; Zhang, Y. An intelligent optimization back-analysis method for geomechanical parameters in underground engineering. *Appl. Sci.* **2022**, *12*, 5761. [CrossRef]

Disclaimer/Publisher's Note: The statements, opinions and data contained in all publications are solely those of the individual author(s) and contributor(s) and not of MDPI and/or the editor(s). MDPI and/or the editor(s) disclaim responsibility for any injury to people or property resulting from any ideas, methods, instructions or products referred to in the content.